*Korean J. Chem. Eng.*, 36(1), 157-165 (2019)
DOI: 10.1007/s11814-018-0200-z

pISSN: 0256-1115
eISSN: 1975-7220

# Synthesis of high-quality carbon nanotubes by using monodisperse spherical mesoporous silica encapsulating iron oxide nanoparticles

**Raji Atchudan*, Bong Geun Cha**, Nasreena Lone*, Jaeyun Kim**,†, and Jin Joo*,†**

*Department of Applied Chemistry, Kyungpook National University, Daegu 41566, Korea
**School of Chemical Engineering, Sungkyunkwan University, Suwon 16419, Korea
(*Received 25 October 2018 • accepted 25 November 2018*)

**Abstract**−Well-graphitized carbon nanotubes (CNTs) were grown by using monodisperse spherical mesoporous silica encapsulating single iron oxide ($Fe_3O_4$) nanoparticles (MSEINPs) as catalytic templates by chemical vapor deposition (CVD) and using acetylene as carbon source. The catalytic templates were synthesized by a sol-gel method. The MSEINPs exhibited better activity and selectivity in CNT synthesis than bare $Fe_3O_4$ catalysts. The synthesized multiwall carbon nanotubes (MWCNTs) were analyzed by powder X-ray diffraction (PXRD), thermogravimetric analysis (TGA), field emission scanning electron microscopy (FESEM), transmission electron microscopy (TEM), and Raman spectroscopy. The carbon deposits are rich in MWCNTs, as confirmed by FESEM and TGA. The wall thickness of the MWCNTs is controlled primarily by the size of the spherical mesoporous silica layer encapsulating the $Fe_3O_4$ NPs, while the inner diameter of the CNTs is determined by the size of the $Fe_3O_4$ NPs at the center of the MSEINPs. The average diameter of the MWCNTs increased significantly with increases in the growth temperature and acetylene flow rate. The analytical results show that the CNTs prepared on MSEINPs are well graphitized with a narrow size distribution in thickness, and straight and longer tubes are obtained without major defects as compared to the CNTs grown on bare $Fe_3O_4$ NPs.

Keywords: Carbon Nanotubes, Mesoporous Silicas, Iron Oxide, Nanoparticles, CVD

## INTRODUCTION

Iijima's landmark paper on a new type of quasi one-dimensional carbon named "carbon nanotubes (CNTs)" attracted a great deal of attention in a wide range of research fields because of the superior mechanical strength, electrical properties, large surface area for hydrogen adsorption, and high aspect ratio of CNTs [1-12]. Three common methods for the synthesis of CNTs are arc discharge [13], laser evaporation [14], and chemical vapor deposition (CVD) [15]. The first two methods employ solid state carbon precursors which are evaporated at high temperature. CVD utilizes hydrocarbon gases as a carbon source with metal nanoparticles as catalytic seeds for the growth of CNTs. CVD methods have enabled us to achieve high yield, selective growth, and vertical alignment during the growth of CNTs. In particular, the catalytic production of CNTs results in a high purity that cannot be achieved by other methods, so that CNTs grown by this method are suitable for many applications, especially in electronics and thermomechanics [16]. Among the variables determining the quality of the final product, the development of an efficient catalyst system underlies the success of CVD processes for synthesizing high quality CNTs. Catalysts such as iron, cobalt, or nickel are often used on supporting materials, which have been found to be a critical factor governing the overall synthesis method.

Mesoporous materials (Mobil Composition of Matter (MCM), Santa Barbara Amorphous (SBA), KIT and others) are promising as catalysts for fine chemical synthesis and as catalyst supports for the production of nanostructured materials because of their large pore volume, high surface area, and narrow pore size distribution. Furthermore, relatively larger pore diameters ranging from 2 to tens of nanometers facilitate molecular diffusion throughout their channels. This makes mesoporous materials one of the best platforms for supporting nano-sized catalysts for growing CNTs and related carbon nanostructures using CVD processes [17-19]. However, several drawbacks are unavoidable in this catalyst system: (i) it is hard to control the thickness of CNTs when the catalyst is loaded into mesoporous channels, (ii) catalyst nanoparticles in mesoporous silica could experience agglomeration at the high temperature conditions of a CVD process, and (iii) it is not a cost-effective process as most of the catalyst nanoparticles deep inside the mesoporous materials can barely participate in CNT growth.

In the present work, we present monodisperse spherical mesoporous silica encapsulating iron oxide nanoparticles (MSEINPs) as a catalytic system to produce CNTs in a highly controllable manner as shown in Fig. 1. Separately prepared $Fe_3O_4$ nanoparticles (NPs) are embedded inside pores of spherical mesoporous silica particles. We study the effect of the growth temperature, growth time, and acetylene flow rate on CNT morphology, investigating the degree of graphitization of CNTs that are controlled by MSEINPs. Control experiments using bare $Fe_3O_4$ NPs as a catalyst were carried out to elucidate the effect of the spherical mesoporous silica supports.

## EXPERIMENTAL METHODS

### 1. Materials

The catalytic templates were synthesized using cetyltrimethylammonium bromide (CTAB, >98%, Aldrich), tetraethylorthosilicate

†To whom correspondence should be addressed.
E-mail: joojin@knu.ac.kr, kimjaeyun@skku.edu

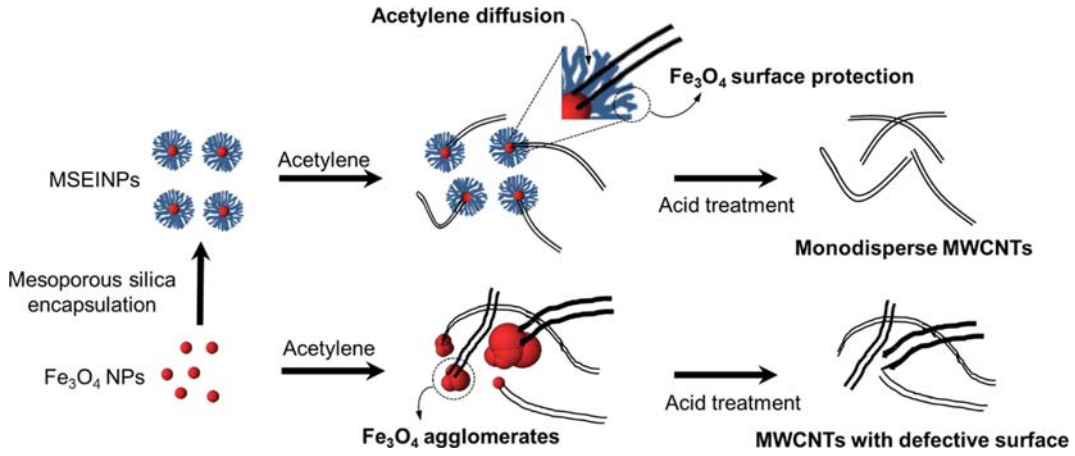


**Fig. 1. Schematic diagram for MWCNTs growth by using MSEINPs and bare $Fe_3O_4$ NPs. Mesoporous silica shell of MSEINPs provides acetylene diffusion path with protecting $Fe_3O_4$ NPs surface.**

(TEOS, 98%, Aldrich), ethyl acetate (99.5%, Dukson), chloroform (99%, Dukson), sodium hydroxide (NaOH, Min. 93%, Dukson), iron(III) chloride ($FeCl_3$, 98%, Aldrich), oleic acid (OA, 90%, Aldrich), and 1-octadecene (90%, Aldrich). The CNTs were synthesized using acetylene (99.5%), argon (99.9%), and hydrogen (99.9%) as a carbon source, carrier gas, and reducing agent, respectively. Hydrofluoric acid (Min. 50%) and hydrochloric acid (35-37%) were purchased from Dukson and were used for purification of the synthesized CNTs. All the chemicals were used without further purification. Deionized (DI) water was used throughout this study.

**2. Synthesis of Catalytic Templates**

The $Fe_3O_4$ NPs capped with oleic acid were synthesized via heat-up process using iron-oleate complex based on the previous report [20]. The MSEINPs were synthesized according to a procedure described in a previous report [21]. Typically, 1.0 mL of $Fe_3O_4$ NPs solution (1.375 mg $Fe_3O_4$/mL) was added to 10 mL of a 0.055 M CTAB solution and stirred vigorously for 30 min. Then, the mixture was heated up to 60 °C and maintained at that temperature for 10 min under stirring to evaporate the chloroform. The resulting solution was mixed with 45 mL of water and 0.3 mL of a 2 M NaOH solution and the mixture was heated up to 70 °C under stirring. Then, 0.5 mL of TEOS and 3 mL of ethyl acetate were added to the reaction mixture in sequence to initiate silica sol-gel reaction. After 3 h, the reaction mixture was centrifuged and washed three times with ethanol. CTAB was extracted from the mesoporous silica nanoparticles by stirring in an acidic ethanolic solution for 3 h at 60 °C. The resulting MSEINPs were washed three times with ethanol and dried at 110 °C. The thickness of mesoporous silica shell was controlled by varying concentrations of TEOS and ethyl acetate. The average estimated sizes of the MSEINPs were 30, 60, 120, and 230 nm; these samples are referred to as, MSEINP-30, MSEINP-60, MSEINP-120, and MSEINP-230 with respect to the size of the mesoporous silica spheres.

**3. Synthesis and Purification of CNTs**

The CVD reaction for the synthesis of CNTs was carried out using the MSEINPs and bare $Fe_3O_4$ NPs as a catalytic template. A simple CVD setup containing a horizontal tubular furnace and gas flow control units are described in Fig. S1. In a typical growth experiment, ~10 mg of each catalytic template was placed in a quartz boat inside a quartz tube. The catalytic template was purged with argon gas at a flow rate of 500 sccm (standard cubic centimeters per minute) for 60 min, followed by hydrogen gas flow at a rate of 200 sccm for 30 min. The reaction was carried out at the desired temperature for 30 min using a mixture of acetylene as a carbon source and argon as a carrier gas at flow rates of 10 and 500 sccm, respectively. The catalytic templates (MSEINP-30, MSEINP-60, MSEINP-120, MSEINP-230, and bare $Fe_3O_4$ NPs), reaction temperatures (700, 750, 800, 850, 900, and 950 °C) and flow rates of acetylene (5, 10, 15, 20, 30, and 50 sccm) were varied to control the CNTs' morphology. The furnace was then cooled to room temperature under an argon atmosphere, and the final product was collected after the completion of the reaction. The obtained samples were treated with hydrofluoric acid and then hydrochloric acid to remove the silica and catalyst nanoparticles. In a typical procedure, the obtained crude CNTs were mixed with hydrofluoric acid and sonicated for 20 min. The sonicated mixture was stirred for 4 h at ambient temperature. The final mixture was filtered and then washed with DI water repeatedly until the pH level of the resulting solution reached ~7.0. This purification step was repeated with hydrochloric acid. The filtered solid black material was dried at 100 °C for 5 h in an oven. Finally, the sample was calcined at 400 °C for 2 h in a muffle furnace to remove any amorphous carbon on the CNTs.

**4. Characterization Methods**

$N_2$ adsorption/desorption isotherms were obtained at 77 K on a Micromeritics ASAP 2020 apparatus. Before analysis, the sample was degassed at 120 °C for about 6 h. Powder X-ray diffraction (PXRD) patterns were obtained on a Rigaku D/MAX-2500 diffractometer using the Cu-K$\alpha$ line ($\lambda$=1.54 Å) as the radiation source, equipped with a liquid nitrogen cooled germanium based solid-state device as the detector. The diffraction intensities were measured over the $2\theta$ range of 5-80° with a step interval of 0.02° and an integration time of 5 s at each step. Thermogravimetric analysis/differential thermal analysis (TGA/DTA) was performed with a TA Instruments SDT Q600 setup. Each sample was heated from 25 to 1,000 °C at a heating rate of 10 °C/min under an air atmosphere. Scanning electron microscopy (SEM) was performed on a Hitachi S-4800 with

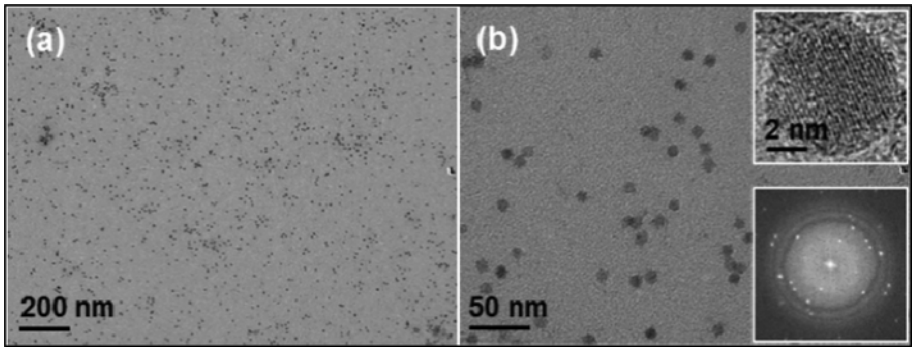


**Fig. 2. TEM images of $Fe_3O_4$ NPs at different magnifications. Insets of (b) show high magnification TEM image of single $Fe_3O_4$ NP (top) and fast Fourier transform (FFT) image from the corresponding TEM image (bottom), which indicate the highly crystalline nature of the $Fe_3O_4$ NPs.**

an acceleration voltage of 4 kV by placing the CNTs on conductive carbon tape. The transmission electron microscope (TEM) images with selected area electron diffraction (SAED) patterns were obtained using a TITAN G2 ChemiSTEM with Probe Cs corrector operated at 200 kV. Samples for TEM analysis were prepared by placing droplets of a suspension of the CNTs in ethanol on a carbon-coated Cu grid. Raman spectra were recorded with an Almega X/Thermo Raman spectrometer using a laser excitation line at 532 nm.

## RESULTS AND DISCUSSION

### 1. Characterization of bare $Fe_3O_4$ NPs and MSEINPs

1-1. Structural Analysis of $Fe_3O_4$ NPs

The morphology of the $Fe_3O_4$ NPs was investigated by TEM analysis. Fig. 2 shows the spherical morphology of the $Fe_3O_4$ NPs with a narrow size distribution. The average diameter of the nanoparticles is 9.2 nm. The insets represent a high-magnification TEM image and fast Fourier transform (FFT) image of the $Fe_3O_4$ NPs, which confirm their highly crystalline nature, which was also revealed by XRD analysis. The PXRD pattern of $Fe_3O_4$ NPs shown in Fig. S2 exhibits a cubic crystal system, well-matched to that of bulk $Fe_3O_4$ (JCPDS No. 88-0315). The intense XRD peaks indicate that the synthesized nanoparticles are highly crystalline in accordance with the TEM analysis and no peaks from impurities are observed [22,23]. The relatively broad peak widths for all diffraction planes result from the finite particle size. The average crystallite size was calculated from the XRD pattern according to the linewidth of the (311) plane diffraction peak using the Debye-Scherrer equation (Eq. (1)):

$$D = \frac{K\lambda}{\beta\cos\theta} \quad (1)$$

where D is the average crystallite size, K is a dimensionless shape factor (0.9), $\lambda$ is the wavelength of the incident X-rays ($\lambda$=1.54 Å), $\beta$ is the full width at half maximum (FWHM) of the diffraction peak, and $\theta$ is the peak position. The average crystallite size of the $Fe_3O_4$ NPs along the (311) plane is estimated to be 9.1 nm which is in good agreement with the mean particle size calculated from the TEM image. This implies that most of the particles are predominantly single crystalline in nature.

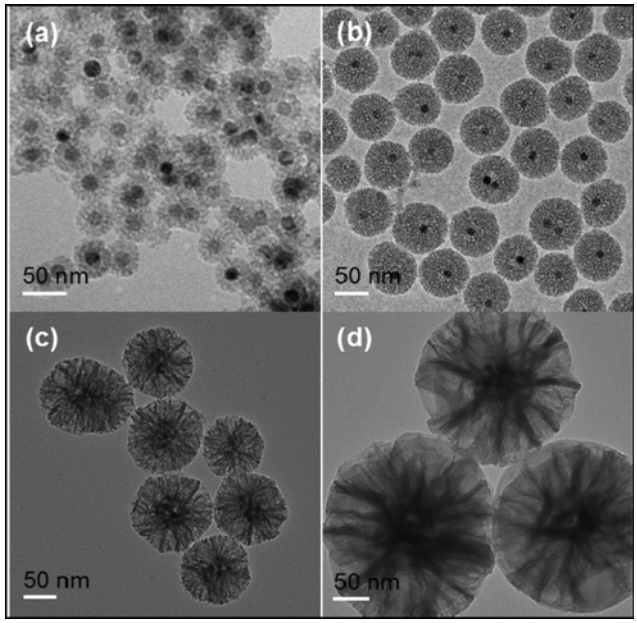


**Fig. 3. TEM images of (a) MSEINP-30, (b) MSEINP-60, (c) MSEINP-120, and (d) MSEINP-230. All the samples have identical $Fe_3O_4$ cores.**

1-2. Structure of MSEINPs

Fig. 3 shows TEM images of the MSEINPs which clearly show that the sample possesses a porous structure with a $Fe_3O_4$ NPs embedded at the center of the mesoporous silica. The pores of the silica are evenly developed in all directions from the centered $Fe_3O_4$ NPs. The average sizes of the MSEINPs estimated from the TEM images in Fig. 3 are 30, 60, 120, and 230 nm, respectively, whereas the average size of the embedded $Fe_3O_4$ NPs is 9.2 nm. Interestingly, the mesoporous channels have a wormhole-like disordered structure. It is well known that such disordered channels are interconnected with each other, leading to fast diffusion of molecules inside the adsorbent. This can be a great advantage in the CVD process, where gaseous carbon sources can easily access the $Fe_3O_4$ catalyst core, promoting CNT growth from the catalyst surface [18,24].

1-3. $N_2$ Adsorption/Desorption Studies of MSEINPs

The $N_2$ adsorption/desorption isotherm of MSEINP-60 is shown

in Fig. S3. The synthesized material exhibited a characteristic type-IV isotherm with a sharp increase in $N_2$ adsorption at relative pressures ranging from 0.3 to 0.4, resulting from well-defined mesoporous channels [25,26]. Barrett-Joyner-Halenda (BJH) calculation shows a narrow size distribution with an average pore diameter of 2.9 nm for MSEINP-60. The Brunauer-Emmett-Teller (BET) specific surface area and pore volume are 770 $m^2$/g and 1.2 $cm^3$/g, respectively. Large adsorption above a relative pressure of 0.9 comes from $N_2$ condensation in secondary pores formed between mesoporous silica particles, as in hexagonal mesoporous silica (HMS) [27].

1-4. Thermogravimetric Analysis of MSEINPs

The thermal stability of MSEINP-60 was examined by TGA/DTA (Fig. S4). Three distinguished weight loss peaks can be observed in the thermogram. The first weight loss observed from 50 to 100 °C is assigned to the removal of surface-absorbed water in the porous host material. The second weight loss began at ~270 °C and ended at ~400 °C due to the decomposition or desorption of oleic acid capping the $Fe_3O_4$ NP surface. This is followed by the third weight loss between 400 and 550 °C, which is ascribed to water loss from the condensation reaction between adjacent silanol (Si-OH) groups to form siloxane bonds [28,29]. Gradual weight loss further proceeds without major decomposition occurring up to 1,050 °C, showing the high thermal stability of our samples. This high thermal stability of the catalyst inside the mesoporous nanoparticles keeps the catalyst $Fe_3O_4$ NPs from being agglomerated at elevated temperatures during the CVD process.

**2. Characterization of Multiwall Carbon Nanotubes (MWCNTs)**

2-1. Morphology of MWCNTs

Figs. 4(a)-(e) displays FESEM images with different magnifications of the as-synthesized MWCNTs grown over MSEINPs with the different sizes and $Fe_3O_4$ NPs under the same CVD conditions. Interestingly, the outer diameter of the CNTs gradually decreases with increasing size of the mesoporous silica sphere. A detailed study of the dependence of their thickness on mesoporous silica size will be provided in the TEM analysis section. These images also clearly illustrate the formation of a large amount of carbon nanotubes over the MSEINP-30 and MSEINP-60 catalysts without any major carbonaceous impurities such as an amorphous or microcrystalline carbon layer. On the other hand, the CNTs grown on the bare $Fe_3O_4$ NPs exhibit highly coiled or bent morphologies and it is hard to define their thickness, as shown in Fig. 4(e). In addition, a considerable amount of impurities can be observed. Figs. 4(f)-(j) show FESEM images with different magnifications of MWCNTs obtained from the various MSEINPs and bare $Fe_3O_4$ NPs after purification. After purification, the majority of the impurities, including the catalytic template of mesoporous silica and iron NPs, were eliminated from the CNTs which can be clearly seen in the FESEM images. The tubular structure of the CNTs remained intact even after acid treatment and the oxidation procedure at temperatures as high as 400 °C. Thus, this confirms that the produced carbon nanotubes are highly graphitic in nature. The thickness distribution of the CNTs becomes narrow as the size of the MSEINPs increases, as shown in Figs. 4(f)-(j).

The growth temperature and flow rate of carbon precursor strongly influence the diameter and morphology of the nanotubes. For this study, we have chosen MSEINP-60 to study the influence of these parameters, as it has the highest production yield and a relatively narrow size distribution. Fig. 5(a) shows SEM images of as-grown MWCNTs on MSEINP-60 with varying growth temperatures from 700 to 950 °C while other conditions were kept constant. The average diameter of the MWCNTs increased from 30 to 120 nm with increasing growth temperature. The surfaces of the CNTs significantly deteriorated as the growth temperature was increased from 700 to 950 °C (Fig. S5(a)). We assume that the rate of acetylene decomposition increases as the growth temperature is increased, resulting in rough, irregular surfaces of the CNTs. This might also be responsible for the increase in the diameter of CNTs. The morphology of CNTs is not much affected by the reaction temperature between 700-850 °C, while an abrupt change in thickness was seen above 900 °C. Moreover, the yield of MWCNTs tends to first increase and then decrease with increasing growth temperature. At lower temperatures (below 750 °C), the inadequate acetylene decomposition results in lower CNT yield [30]. At higher temperatures above 900 °C, the formation of MWCNTs decreases while the formation of CNTs with defective surfaces increases due to the self-pyrolysis of MWCNTs.

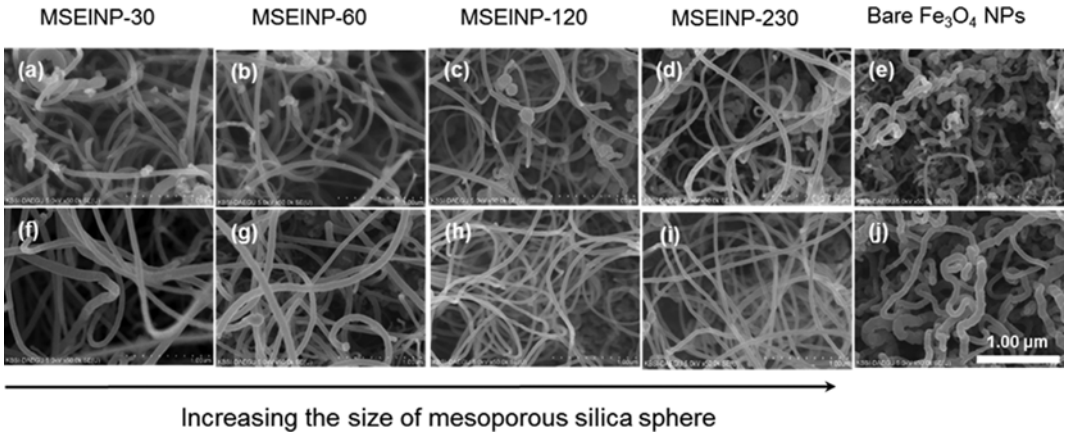


**Fig. 4. SEM images of the as-grown and purified MWCNTs over (a) and (f) MSEINP-30; (b) and (g) MSEINP-60; (c) and (h) MSEINP-120; (d) and (i) MSEINP-230; (e) and (j) bare $Fe_3O_4$ NPs. CVD conditions were the same for all the samples: growth time was 30 min, flow rate of acetylene/Ar gas was 10 sccm/500 mL·$min^{-1}$, temperature was set at 800 °C.**

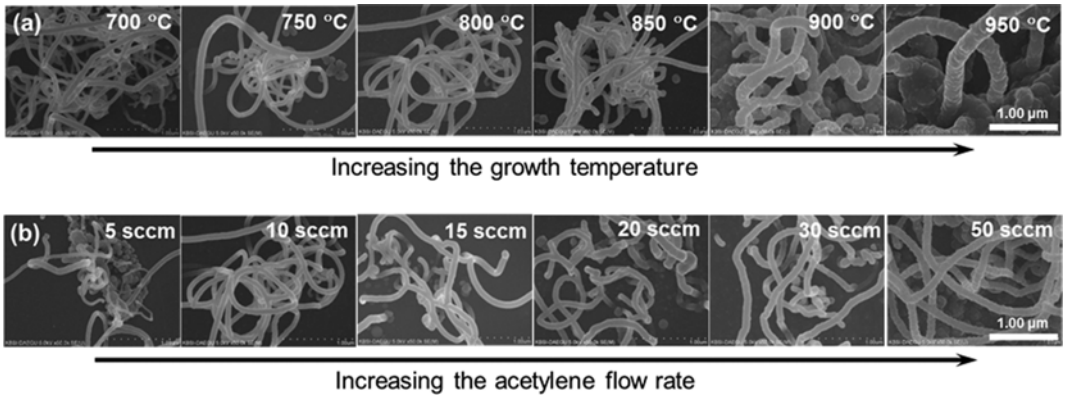


**Fig. 5. (a) SEM images of the MWCNTs grown over MSEINP-60 with 10 sccm of acetylene flow for 30 min at different temperatures from 700 to 950 °C. (b) SEM images of the MWCNTs grown over MSEINP-60 with a acetylene flow rate from 5 sccm to 50 sccm for 30 min. Growth temperature was set at 800 °C with an Ar-flow rate of 500 mL/min.**

The flow rate of carbon precursor is another crucial factor affecting the growth and surface morphology of CNTs. In order to elucidate this effect, the flow rate of the carbon precursor was altered from 5 to 50 sccm during CNT growth over MSEINP-60. Fig. 5(b) shows that the average diameter of the MWCNTs gradually increased with increasing flow of acetylene ($C_2H_2$) gas. The image also shows that the roughness of the surface increased as the gas flow was increased from 5 to 50 sccm. Individual CNTs and the surface roughness can be clearly observed in the high magnification SEM images (Fig. S5(b)). The roughness of the nanotube becomes significant with higher flow rates because of the increase in the amorphous nature of the graphitic layer deposited during the formation of the MWCNTs. The change in the surface morphology of the CNTs was not significant at flow rates up to 30 sccm, but the surface morphology was significantly affected at flow rates around 50 sccm (the degree of graphitization will be discussed along with the Raman spectroscopy characterization in section 2.2).

Figs. 6(a) and (b) demonstrate that multi-walled CNTs were grown from MSEINP-60 placed at the center of MSEINPs. It is apparent that the inner diameter of the MWCNTs is determined by the size of the $Fe_3O_4$ nanoparticles (9.2 nm), not by the size of the mesoporous silica sphere. The dependence of the inner diameter of the CNTs on the $Fe_3O_4$ NPs inside the silica spheres is consistent throughout all the MSEINP samples (MSEINP-30, MSEINP-60, MSEINP-120 and MSEINP-230), regardless of silica size. In contrast, the outer diameter of the MWCNTs slightly decreased with increasing mesoporous silica sphere size, which means the thick-

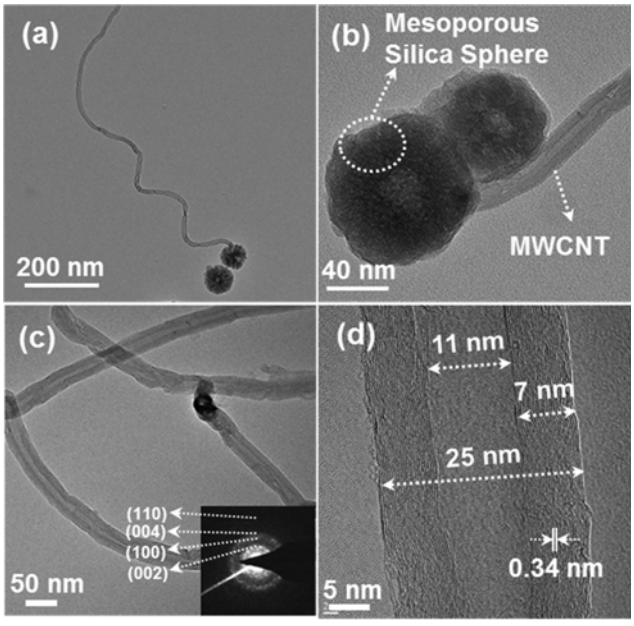


**Fig. 6. TEM images of as-grown MWCNTs ((a) and (b)) and purified MWCNTs ((c) and (d)) at different magnifications grown on MSEINP-60 with 10 sccm of acetylene flow for 30 min at 800 °C. Inset of (c) represents SAED pattern of MWCNTs after purification.**

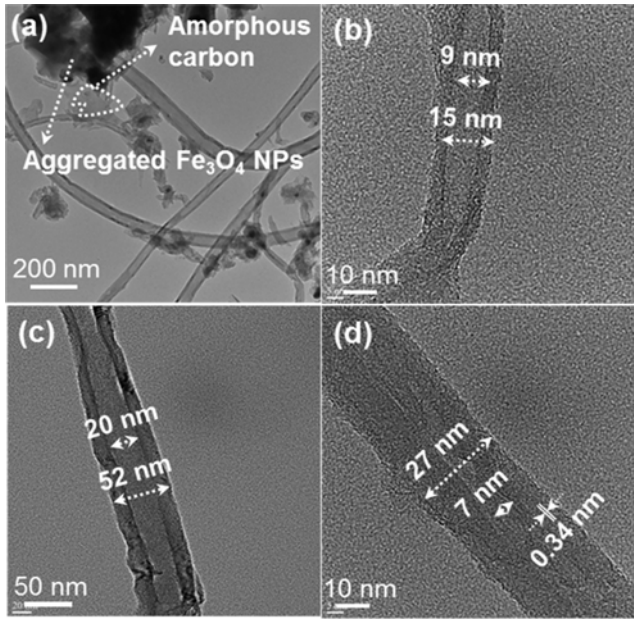


**Fig. 7. (a) TEM images of as-grown MWCNTs on bare $Fe_3O_4$ NPs with 10 sccm of acetylene flow for 30 min at 800 °C. (b)-(d) HRTEM images of MWCNTs corresponding sample shown in (a).**

ness of the silica shell controls the outer layer of the MWCNTs during growth. The HRTEM image and SAED pattern presented in Figs. 6(c) and (d) indicate a high degree of graphitization of the synthesized CNTs. Interlayer distances (distance between two graphene layers) estimated from HRTEM images are 0.34 nm for MWCNTs obtained from MSEINP-30 and MSEINP-60. Fig. 7(a) shows TEM images of as-grown MWCNTs on the bare $Fe_3O_4$ NPs. A considerable amount of carbonaceous impurities are observed, along with irregularly shaped MWCNTs. In this case, the inner diameter of the CNTs is not determined by the catalyst size and a broad diameter distribution is observed. This could presumably be due to aggregation between nanoparticles during the MWCNT growth as shown in Fig. 7(a). The high surface energy due to the high curvature of the nanoparticle surface would accelerate the aggregation process. This aggregation process of catalyst particles necessarily causes a broad diameter distribution in the produced CNTs when the bare $Fe_3O_4$ NPs are used as a catalyst. We believe that our method of employing a mesoporous silica shell around the catalyst for CNT growth is superior to other catalytic systems in terms of the monodispersity of the resulting CNTs, and is promising for mass production. HRTEM images of MWCNTs corresponding to the sample in Fig. 7(a) are shown in Figs. 7(b)-(d). This clearly shows the broad size distribution of the inner and outer diameters of the MWCNTs.

2-2. Raman Spectroscopy Analysis

Raman spectra are presented in Fig. 8 for samples of the MWCNTs obtained from different catalytic templates. MWCNTs usually have two common bands below 2,000 $cm^{-1}$ in their Raman spectrum (*i.e.*, D-band and G-band) [31]. The D-band is related to the defects in the graphitic sheets and the G-band to the vibration of the $sp^2$-hybridized carbon atoms in the graphitic sheets. The disorder-induced D-band occurred at ~1,340 $cm^{-1}$ and the G-band was observed at ~1,580 $cm^{-1}$ for all the samples [32]. The absence of radial breathing modes (RBMs) was also noted for all the samples when

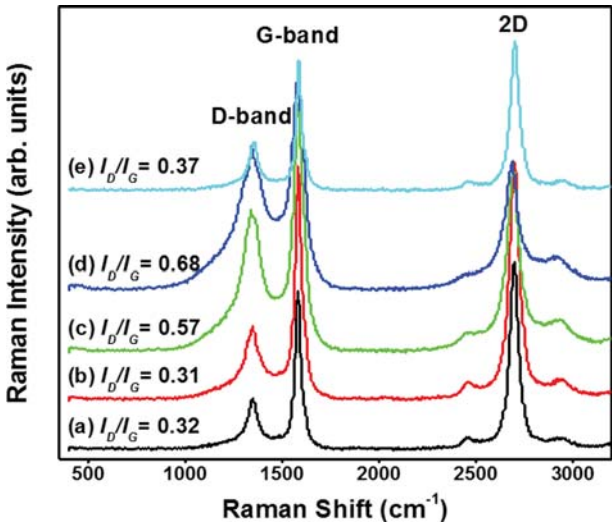


**Fig. 8. Raman spectra of the MWCNTs grown over (a) MSEINP-30, (b) MSEINP-60, (c) MSEINP-120, (d) MSEINP-230, and (e) bare $Fe_3O_4$ NPs with 10/500 sccm of acetylene/Ar flow for 30 min at 800 °C.**

scans were performed below 500 $cm^{-1}$. The absence of RBMs confirms that the obtained nanotubes are exclusively MWCNTs and not SWCNTs. The intensities of the D-band and G-band are denoted as $I_D$ and $I_G$, respectively. The $I_D/I_G$ ratio is used as a measure of the degree of graphitization [33,34]. A lower intensity ratio of D to G band ($I_D<I_G$) indicates a higher degree of graphitization of the obtained CNTs [35-37]. $I_D/I_G$ values of 0.32, 0.31, 0.57, 0.68 and 0.37 were obtained for MWCNTs synthesized from MSEINP-30, MSEINP-60, MSEINP-120, MSEINP-230, and bare $Fe_3O_4$, respectively. Increases in the $I_D/I_G$ values with increasing size of the mesoporous silica spheres from MSEINP-30 to MSEINP-230 can be clearly seen in the Raman spectra.

To examine the effects of growth temperature and gas flow rate on the degree of graphitization, Raman spectra were collected for samples synthesized under different conditions. When the growth temperature was set at 700, 750, 800, 850, 900, and 950 °C, the $I_D/I_G$ values were estimated to be 0.52, 0.41, 0.31, 0.45, 0.80, and 0.86, respectively (Fig. S6). Acetylene flow rate has a similar effect on the $I_D/I_G$ ratio. $I_D/I_G$ values of around 0.32, 0.31, 0.31, 0.39, 0.45 and 0.73 were observed for acetylene flow rates of 5, 10, 15, 20, 30 and 50 sccm, respectively (Fig. S7). A synthesis temperature ranging from 750 to 850 °C and a flow rate of acetylene between 5 and 15 sccm have no appreciable effect on the graphitization. This is in good agreement with the SEM analysis in Figs. 5 and S5. It is obvious that the CNT surface begins to be rough above a growth temperature of 900 °C. Likewise, flow rates higher than 20 sccm create a substantial amount of defects on the graphitic surfaces of CNTs. As mentioned above, an $I_D/I_G$ value of less than 1 indicates a high graphitic degree of carbon. Among all the catalytic templates examined in this study (MSEINP-30, MSEINP-60, MSEINP-120, MSEINP-230, and INP), carbon nanotubes produced from the MSEINP-60 showed the highest degree of graphitization ($I_D/I_G$=0.31), achieving a reasonable yield. The disorder-induced defect formation is related to the creation of carbonaceous impurities such as amorphous and microcrystalline carbon. These impurities could interfere with the formation of graphene layers during CNT growth. An elevated temperature or a high acetylene flow rate provides a configuration where a lot of impurities are produced, leading to defect formation in the MWCNTs [38,39].

2-3. Thermogravimetric Analysis

TGA/DTA studies of as-grown MWCNT over the various sizes of MSEINPs and bare $Fe_3O_4$ NPs were carried out from 20 to 1,000 °C in air atmosphere and the results are shown in Fig. 9(a). The weight loss observed from 550 to 700 °C corresponds to the thermal decomposition of MWCNTs. There was no weight loss above 700 °C and the residual mass is ascribed to MSEINPs containing silica and $Fe_3O_4$ NPs. There is no characteristic weight loss of amorphous carbon observed for MWCNTs obtained over the MSEINPs. Therefore, TGA confirms the high purity of the MWCNTs (~100%) and the lack of carbonaceous impurities such as amorphous carbon, microcrystalline carbon, or CNTs with structural defects on the catalytic templates.

The highest thermal decomposition temperature of as-grown MWCNTs on the MSEINPs slightly decreased with increases in the size of the MSEINPs, which is clearly seen in the DTA curves (Fig. 9(a)). This could presumably be due to the low degree of graphiti-

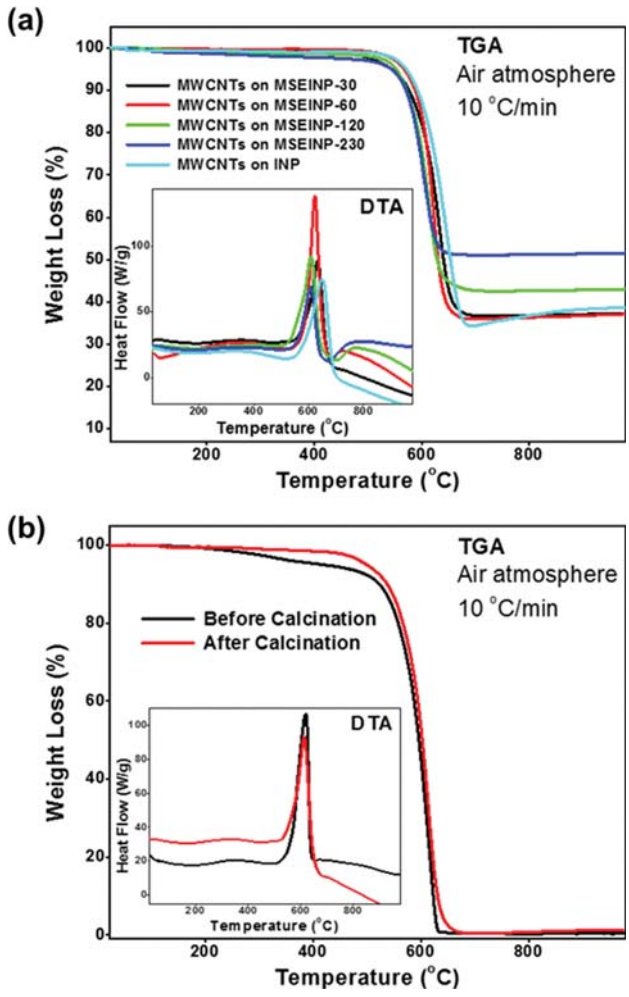


**Fig. 9. TGA/DTA curves of (a) the as-grown MWCNTs over different MSEINPs and bare $Fe_3O_4$ NPs and (b) the purified MWCNTs (before and after calcination) grown over MSEINP-60 with 10 sccm of acetylene flow for 30 min at 800 °C.**

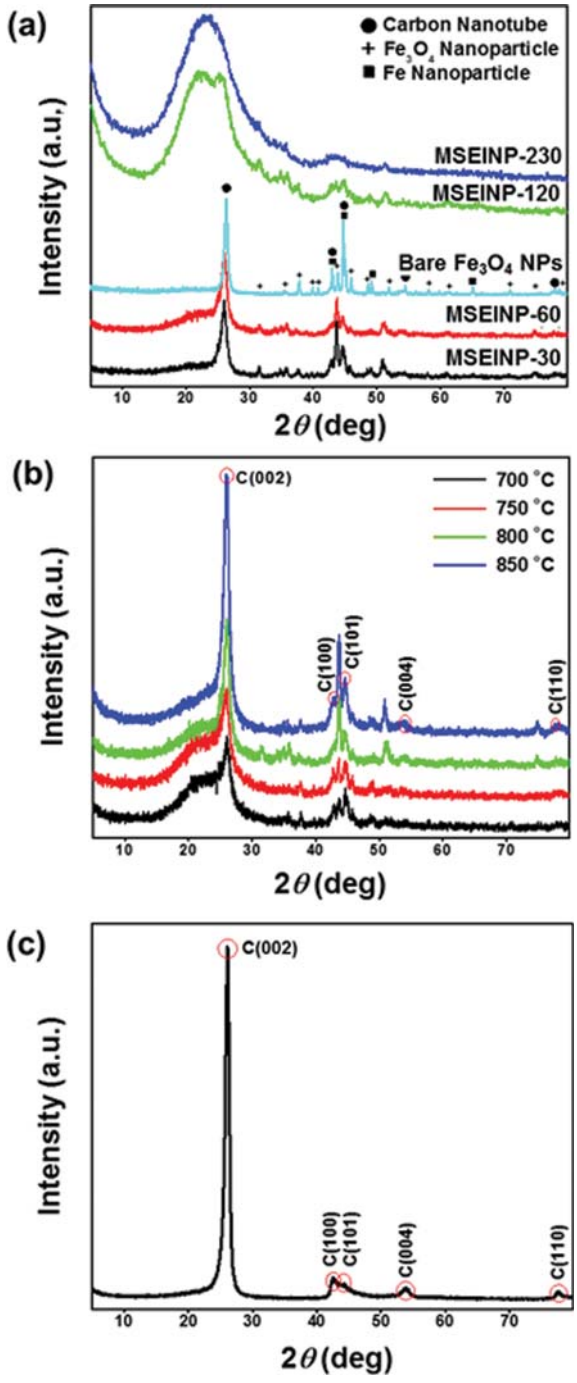


**Fig. 10. XRD patterns of (a) the as-grown MWCNTs over various catalytic templates of MSEINPs, (b) the as-grown MWCNTs grown over MSEINP-60 synthesized at various temperature, and (c) the purified MWCNTs obtained over MSEINP-60. All samples were prepared with 10 sccm of acetyelen flow for 30 min at 800 °C.**

zation of MWCNTs produced from larger MSEINP catalysts. As mentioned above, the outer diameter of the MWCNTs decreased with increasing MSEINP size while the average inner diameters of the MWCNTs are similar for all samples obtained from different sizes of MSEINPs (from MSEINP-30 to MSEINP-230). In general, the thermal stability of MWCNTs is enhanced by a larger number of graphene layers. In this regard, CNTs from MSEINPs with thicker mesoporous silica shells tend to have lower thermal stability. For example, MSEINP-230 produced MWCNTs with a thinner outer diameter while the inner diameter was the same as that from MSEINP-30. The TGA/DTA curves of acid-treated MWCNTs obtained over the MSEINP-60 with 10 sccm of acetylene flow for 30 min at 800 °C, before and after calcination are shown in Fig. 9(b). After acid treatment, no residue of the MWCNTs was observed above ~700 °C, which confirms the complete removal of the catalytic templates (MSEINP-60), leaving behind pure MWCNTs [40]. Before calcination of the as-prepared samples, the carbon material was completely oxidized to form gaseous $CO_2$ and CO by heating in air. The decomposition temperature between 550 and 700 °C can be attributed to the oxidation of MWCNTs. The weight loss between 350 and 450 °C can be attributed to the combustion of amorphous carbon. The as-grown MWCNTs grown over the MSEINP-60 catalyst showed no weight loss from 350 to 450 °C [41]. After acid treatment, carbonaceous impurities were present (around 5%) which can be clearly seen in the thermogram (Fig. 9(b)), implying

that carbonaceous impurities were formed during the acid treatment. These impurities come from the damage to the side walls and outer layer of the MWCNTs caused by the HF and HCl treatments used to remove the silica and the $Fe_3O_4$ NPs encapsulated by mesoporous silica. The damaged carbon is decomposed between 350 and 450 °C. After calcination, only a single weight loss occurred between 550 and 700 °C. These results strongly suggest that the calcination process helps to remove the carbonaceous impurities, giving CNTs with 100% purity.

2-4. XRD Analysis

PXRD patterns of as-grown MWCNTs over the various MSEINPs and bare $Fe_3O_4$ NPs with 10 sccm of acetylene flow for 30 min at 800 °C are shown in Fig. 10(a). The strongest diffraction peak at around 26° was indexed to the (002) plane, while the peaks at ~42 and 44° were indexed to the (100) and (101) planes, respectively. Weaker peaks were observed at around 54 and 78° corresponding to the (004) and (110) planes, respectively. This spectrum reveals a characteristic pattern of a typical graphite structure [42]. The graphitic peaks and the metal Fe NP peaks are labelled in the XRD patterns. The diffraction peak from the (002) plane is clear for the MWCNTs obtained over the MSEINP-30, MSEINP-60, and bare $Fe_3O_4$ NPs. In the case of the XRD pattern of the sample from MSEINP-230, a broad silica peak by short range order is predominant. This might result from the low degree of graphitization of the MWCNTs, which is in good agreement with the Raman spectroscopy analysis. PXRD patterns of the as-grown MWCNTs over the MSEINP-60 catalyst with 10 sccm of acetylene flow for 30 min at various temperatures, are shown in Fig. 10(b). The metal Fe peaks also gradually increased as the reaction temperature was increased due to the faster reduction rate of $Fe_3O_4$ NPs at higher temperatures. Fig. 10(c) depicts a typical XRD pattern of the purified MWCNTs which were obtained from the MSEINP-60 catalyst with 10 sccm of acetylene flow for 30 min at 800°C. All the peaks are well matched with the hexagonal graphite structure, with the diffraction peaks of graphite observed at about 42.6, 44.3, 53.8 and 77.6°, associated with the C(100), C(101), C(004) and C(110) diffractions of CNTs, respectively [43,44]. The characteristic peaks of impurities (silica and $Fe_3O_4$ NPs) disappeared after the purification step, leaving an XRD pattern of pure MWCNTs. The interlayer distance between the (002) planes was calculated to be 0.34 nm for the purified MWCNTs, which is in accordance with the interlayer distance obtained from HRTEM images (Fig. 6(d)). This result strongly suggests that the obtained MWCNTs are highly pure after thorough purification.

**3. CNTs Growth Process Inside MSEINPs**

Experiments for the synthesis of CNTs were carried out with MSEINPs and bare $Fe_3O_4$ NPs. When $Fe_3O_4$ NPs are encapsulated by mesoporous silica, high quality MWCNTs with narrow size distribution are produced, while CNTs with a broad size distribution were obtained using the bare $Fe_3O_4$ NPs. This study suggests that the size distribution of CNTs can be finely tuned by using catalyst particles embedded in mesoporous silica. The mechanism behind the formation of CNTs is as follows: acetylene gas produces carbon radicals at an elevated temperature. The produced carbon radicals form Fe-C bonds at the active sties of $Fe_3O_4$ NPs inside the mesoporous silica. In the meantime, a large flux of carbon radicals into the centers of the MSEINPs via large pores provides enough monomers to grow CNTs at the active sites where Fe-C bonds have formed. This results in the extension of the growing CNTs toward the outside of the mesoporous silica because of the high catenation properties of carbon radicals, while the mesoporous silica surrounding the catalyst core prevents the $Fe_3O_4$ NPs in the core from being agglomerated [45]. The inner diameter of the obtained CNTs is therefore strongly correlated with the size of the $Fe_3O_4$ NPs within the mesoporous silica shell. When bare $Fe_3O_4$ NPs are used as a catalyst, they would undergo significant agglomeration at high temperatures, and therefore no correlation between inner diameter of CNTs and the size of the catalyst for CNT growth is observed. The beneficial effect of the mesoporous silica shell impacts the distribution of outer diameters of the CNTs obtained from MSEINPs, ranging from 25 to 30 nm. In contrast, CNTs obtained from $Fe_3O_4$ NPs have diameters in the range from 15 to 45 nm.

## CONCLUSION

A new catalyst system has been explored for producing high quality MWCNTs by using mesoporous silica encapsulating iron oxide nanoparticles by a CVD method. Single $Fe_3O_4$ NPs are embedded at the centers of mesoporous silica spheres which are used as an excellent catalytic platform: the catalyst NPs are never aggregated at high temperatures during the CVD process and the thickness of the produced CNT is controlled by the $Fe_3O_4$ NPs and mesoporous silica shell thickness, yielding high quality CNTs. The uniform pores of the MSEINPs make them suitable for preparing CNTs because the channels leading to the core $Fe_3O_4$ NPs facilitate the diffusion of gas-phase carbon precursors. In this regard, thin mesoporous silica shell should be better in terms of acetylene diffusion into catalyst core rather than micrometer-thick silica shell. In addition, overcoating the catalyst NPs with silica provides great stability at high temperatures. The size of the MSEINPs, the flow rate of the carbon precursor, and the reaction temperatures were systematically studied to control the size distribution and quality of the MWCNTs. MWCNTs were obtained from MSEINPs without any carbonaceous impurities. All the analytical results strongly support the conclusion that the MWCNTs produced over the MSEINPs are well graphitized with a narrow size distribution. The preparation of CNTs with high purity and a narrow size distribution is critical for many potential applications. The catalyst system for CNT production described in this study will be an ideal choice for future CNT applications.

## ACKNOWLEDGEMENTS

This Research was supported by Kyungpook National University Research Fund, 2015 and a grant funded by the National Research Foundation under the Ministry of Science and ICT, Republic of Korea (2014M3A9B8023471).

## SUPPORTING INFORMATION

Additional information as noted in the text. This information is available via the Internet at http://www.springer.com/chemistry/journal/11814.

## REFERENCES


1. S. Iijima, *Nature*, **354**, 56 (1991).
2. S. Iijima and T. Ichihashi, *Nature*, **363**, 603 (1993).
3. A. A. Koval'chuk, A. N. Shchegolikhin, V. G. Shevchenko, P. M. Nedorezova, A. N. Klyamkina and A. M. Aladyshev, *Macromolecules*, **41**, 3149 (2008).
4. M. M. Rahman, R. Suleiman and H. D. Kim, *Korean J. Chem. Eng.*, **34**, 2480 (2017).
5. W.-J. Lee, S. Jeong, H. Lee, B.-J. Kim, K.-H. An, Y.-K. Park and S.-C. Jung, *Korean J. Chem. Eng.*, **34**, 2993 (2017).
6. C. Liu and H. M. Cheng, *Mater. Today*, **16**, 19 (2013).
7. M. F. L. De Volder, S. H. Tawfick, R. H. Baughman and A. John Hart, *Science*, **339**, 535 (2013).
8. N. Azizi, M. Arzani, H. R. Mahdavi and T. Mohammadi, *Korean J. Chem. Eng.*, **34**, 2459 (2017).
9. L. Yang, Y. An, B. Dai, X. Guo, Z. Liu and B. Peng, *Korean J. Chem. Eng.*, **33**, 2271 (2016).
10. Z. Shadike, M. H. Cao, F. Ding, L. Sang and Z. W. Fu, *Chem. Commun.*, **51**, 10486 (2015).
11. R. Atchudan and A. Pandurangan, *Micropor. Mesopor. Mater.*, **167**, 162 (2013).
12. S. U. Rather, *Korean J. Chem. Eng.*, **33**, 1511 (2016).
13. D. S. Bethune, C. H. Kiang, M. S. de Vries, G. Gorman, R. Savoy, J. Vazquez and R. Beyers, *Nature*, **363**, 605 (1993).
14. T. Guo, P. Nikolaev, A. Thess, D. T. Colbert and R. E. Smalley, *Chem. Phys. Lett.*, **243**, 49 (1995).
15. V. Ivanov, J. B. Nagy, P. Lambin, A. Lucas, X. B. Zhang, X. F. Zhang, D. Bernaerts, G. Van Tendeloo, S. Amelinckx and J. Van Landuyt, *Chem. Phys. Lett.*, **223**, 329 (1994).
16. J. Balamurugan, A. Pandurangan, N. H. Kim and J. H. Lee, *Nanoscale*, **7**, 679 (2015).
17. R. Atchudan, J. Joo and A. Pandurangan, *Mater. Res. Bull.*, **48**, 2205 (2013).
18. F. Zheng, L. Liang, Y. Gao, J. H. Sukamto and C. L. Aardahl, *Nano Lett.*, **2**, 729 (2002).
19. R. Atchudan, A. Pandurangan and J. Joo, *Micropor. Mesopor. Mater.*, **175**, 161 (2013).
20. J. Park, K. An, Y. Hwang, J. G. Park, H. J. Noh, J. Y. Kim, J. H. Park, N. M. Hwang and T. Hyeon, *Nature Mater.*, **3**, 891 (2004).
21. J. Kim, H. S. Kim, N. Lee, T. Kim, H. Kim, T. Yu, I. C. Song, W. K. Moon and T. Hyeon, *Angew. Chem. Int. Ed.*, **47**, 8438 (2008).
22. J. Mohapatra, A. Mitra, D. Bahadur and M. Aslam, *CrystEngComm*, **15**, 524 (2013).
23. X. Huang, A. Schmucker, J. Dyke, S. M. Hall, J. Retrum, B. Stein, N. Remmes, D. V. Baxter, B. Dragnea and L. M. Bronstein, *J. Mater. Chem.*, **19**, 4231 (2009).
24. P. Ramesh, T. Okazaki, R. Taniguchi, J. Kimura, T. Sugai, K. Sato, Y. Ozeki and H. Shinohara, *J. Phys. Chem. B*, **109**, 1141 (2005).
25. Y. Xiao, T. Wang, Y. Cao , X. Wang , Y. Zhang, Y. Liu and Q. Huo, *Dalton Trans.*, **44**, 4355 (2015).
26. R. Atchudan, A. Pandurangan and T. Somanathan, *J. Mol. Catal A: Chem.*, **309**, 146 (2009).
27. T. R. Pauly and T. J. Pinnavaia, *Chem. Mater.*, **13**, 987 (2001).
28. C. Y. Chen, H. X. Li and M. E. Davis, *Micropor. Mater.*, **2**, 17 (1993).
29. M. L. Occelli, S. Biz, A. Auroux and G. J. Ray, *Micropor. Mesopor. Mater.*, **26**, 193 (1998).
30. N. Halonen, K. Kordás, G. Tóth, T. Mustonen, J. Mäklin, J. Vähäkangas, P. M. Ajayan and R. Vajtai, *J. Phys. Chem. C*, **112**, 6723 (2008).
31. A. C. Ferrari and J. Robertson, *Phys. Rev. B*, **61**, 14095 (2000).
32. Z. Iatridi and C. Tsitsilianis, *Soft Matter*, **9**, 185 (2013).
33. A. A. Mamedov, N. A. Kotov, M. Prato, D. M. Guldi, J. P. Wicksted and A. Hirsch, *Nat. Mater.*, **1**, 190 (2002).
34. R. Zhang and X. Wang, *Chem. Mater.*, **19**, 976 (2007).
35. R. Atchudan, S. Perumal, D. Karthikeyan, A. Pandurangan and Y. R. Lee, *Micropor. Mesopor. Mater.*, **215**, 123 (2015).
36. W. Li, L. S. Zhang, Q. Wang, Y. Yu, Z. Chen, C. Y. Cao and W. G. Song, *J. Mater. Chem.*, **22**, 15342 (2012).
37. R. Atchudan and A. Pandurangan, *J. Mol. Catal A: Chem.*, **355**, 75 (2012).
38. S. Vetrivel, J. S. Do, M. Y. Cheng and B. J. Hwang, *J. Phys. Chem. C*, **111**, 16211 (2007).
39. M. Escobar, M. S. Moreno, R. J. Candal, M. C. Marchi, A. Caso, P. I. Polosecki, G. H. Rubiolo and S. Goyanes, *Appl. Sur. Sci.*, **254**, 251 (2007).
40. K. Chajara, C. H. Andersson, J. Lu, E. Widenkvist and H. Grennberg, *New J. Chem.*, **34**, 2275 (2010).
41. S. Scaccia, M. Carewska and P. P. Prosini, *Thermochim. Acta*, **435**, 209 (2005).
42. R. Atchudan, S. Perumal, T. N. J. I. Edison and Y. R. Lee, *RSC Adv.*, **5**, 93364 (2015).
43. J. Sui, C. Zhang, D. Hong, J. Li, Q. Cheng, Z. Lib and W. Cai, *J. Mater. Chem.*, **22**, 13674 (2012).
44. J. C. Juan, Y. Jiang, X. Meng, W. Cao, M. A. Yarmo and J. C. Zhang, *Mater. Res. Bull.*, **42**, 1278 (2007).
45. D. Yuan, X. Yuan, W. Zou, F. Zeng, X. Huang and S. Zhou, *J. Mater. Chem.*, **22**, 17820 (2012).